Photo−Click Chemistry to Design Highly Efficient Lanthanide β−Diketonate Complexes Stable under UV Irradiation

7 AUTHORS, INCLUDING:

P. P. Lima

42 PUBLICATIONS 809 CITATIONS

SEE PROFILE

Mariela Martins Nolasco

University of Aveiro

28 PUBLICATIONS 362 CITATIONS

SEE PROFILE

Rute A Sá Ferreira

University of Aveiro

336 PUBLICATIONS 6,201 CITATIONS

SEE PROFILE

Luís D Carlos

University of Aveiro

483 PUBLICATIONS 9,760 CITATIONS

SEE PROFILE

Photo−Click Chemistry to Design Highly Efficient Lanthanide β-Diketonate Complexes Stable under UV Irradiation

Patrícia P. Lima,[†] Mariela M. Nolasco,[‡] Filipe A. A. Paz,[‡] Rute A. S. Ferreira,[†] Ricardo L. Longo,*,[§] Oscar L. Malta,[§] and Luís D. Carlos*,[†]

[†]Department of Physics and CICECO, Universidade de Aveiro, 3810-193 Aveiro, Portugal
[‡]Department of Chemistry and CICECO, Universidade de Aveiro, 3810-193 Aveiro, Portugal
[§]Departamento de Química Fundamental, Universidade Federal de Pernambuco, Cidade Universitária, Recife-PE, 50740-560, Brazil

S *Supporting Information*

ABSTRACT: Europium (*t*-**Eu**) and gadolinium (*t*-**Gd**) β-diketonate complexes with photoactive *t*-bpete ligand, [Ln-(btfa)$_3$(*t*-bpete)(MeOH)] (Ln = Eu, Gd), where btfa$^-$ and *t*-bpete are 4,4,4-trifluoro-1-phenyl-1,3-butanedionate and *trans*-1,2-bis(4-pyridyl)ethylene, respectively, were synthesized, characterized by vibrational, absorption (reflectance) and photoluminescence spectroscopies and their crystal structure was determined using single-crystal X-ray diffraction. B3LYP calculations were performed to support the interpretation and rationalization of the experimental results. The complexes, under UV irradiation, do not display the typical photodegradation of the β-diketonate ligands exhibiting, in turn, an unprecedented photostability during, at least, 10 h. During UV-A exposure (>330 nm), the emission intensities of both complexes increase drastically (∼20 times), whereas for *t*-**Eu** the emission quantum yield is enhanced at least 30-fold. A mechanism based on a photoclick trans-to-cis isomerization of both *t*- and *c*-bpete moieties was proposed to explain the abnormal photostability of these compounds, either in solid state or in solution. The experimental and computational results are consistent with a photostationary state involving the trans-to-cis isomerization of the bpete ligand under continuous UV-A exposure, which thus diverts the incident radiation from other deleterious photochemical or photophysical processes that cause the typical photobleaching behavior of chelate lanthanide complexes. This shielding mechanism could be extended to other ligands permitting the design of new lanthanide-based photostable systems under UV exposure for applications in lighting, sensing, and displays.

KEYWORDS: *Eu^{3+} and Gd^{3+} complexes, trans-to-cis photoisomerization, trans-1,2-bis(4-pyridyl)ethylene, luminescence intensity and quantum yield enhancement, photostability mechanism, degradation under UV irradiation*
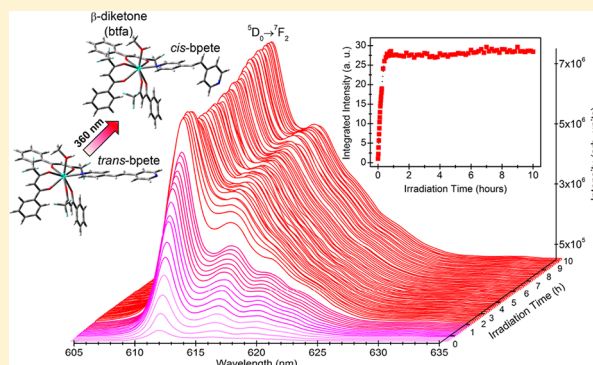
■ INTRODUCTION

Trivalent lanthanide ions (Ln^{3+}) form complexes with various organic molecules, such as aromatic β-diketonates,[1,2] carboxylic acids,[3,4] calixarenes,[5] cryptands,[6] podands,[7] and macrocyclic ligands,[8] emitting efficiently in the near-UV (Ce^{3+} and Gd^{3+}), visible (blue, Tm^{3+}; green, Tb^{3+} and Er^{3+}; yellow, Dy^{3+}; orange, Sm^{3+}; red, Er^{3+}, Eu^{3+}), and near-infrared (Nd^{3+}, Er^{3+}, Tm^{3+}, and Yb^{3+}) spectral regions. These chromophores typically present effective absorption cross sections 10^4−10^5 times higher (and over a much broader spectral range) than the Ln^{3+} corresponding ones, shielding the metal ions from deleterious quenching interactions (e.g., with solvent molecules). The absorbed energy is efficiently transferred to nearby Ln^{3+} centers, which in turn undergo a radiative emitting process, the so-called lanthanide luminescence sensitization, or antenna effect, in analogy to light harvesting molecules found in photosynthetic systems.

The interest in these materials has steadily grown in the last two decades due to their wide range of potential photonic applications, such as tunable lasers,[9] amplifiers for optical communications,[10] components of the emitter layers in multilayer organic light-emitting diodes (OLEDs),[11] luminescent labels in advanced time-resolved fluoroimmunoassays,[12] light concentrators for photovoltaic devices,[13] MRI contrast agents,[14] and luminescent thermometers.[15] Several comprehensive reviews on the subject have been published over the last 12 years reflecting the intense research activity performed.[2,3,5,16–18]

The rather low photostability under UV irradiation of the Ln^{3+} complexes has contributed to exclude these materials from a widely practical use in lighting, sensing, and displays. This

photodegradation process has been observed in lanthanide complexes with β-diketonate chelates,[2,19−25] carboxylic acid derivatives,[26−28] cryptands,[29] and methaneseleninate ligands.[30] Although often attributed to photobleaching, photon-induced chemical damage, or intermolecular H-bond interactions,[21,24,31,32] the photodegradation mechanism has not yet been elucidated. Moreover, for β-diketonates it is independent of the type of the ligand, being observed for both aromatic (e.g., btfa, tta and nta, where btfa⁻, tta⁻, and nta⁻ stands for 4,4,4-trifluoro-1-phenyl-1,3-butanedionate, 4,4,4-trifluoro-1-(2-thienyl)-1,3-butanedionate, and 4,4,4-trifluoro-1-(2-naphthyl)-1,3-butanedionate, respectively)[22,33] or nonaromatic (e.g., acac, where acac⁻ denotes acetylacetonate)[25,34] molecules. It is interesting that photodegradation was used to develop irreversible sensor dosimeters within the three main UV regions related to skin-damage effects: UV-A (365 nm), UV-B (315 nm), and UV-C (290 nm).[3,20,35] Moreover, recently, Quirino et al. developed an OLED using an Eu³⁺ β-diketonate complex whose emission is inversely proportional to the UV irradiation exposure thus allowing its use as a portable UV personal dosimeter.[11]

To the best of our knowledge, there is only one example reported in the literature showing a slight intensification during a short period of time of the intra4f^8 emission in [Tb-(btfa)₃phen] (where phen is 1,10-phenanthroline) under continuous UV-B (315 nm) irradiation.[35] However, it is worth mentioning that after ∼25 min under continuous irradiation the emission intensity starts to decrease following the typical photobleaching process of β-diketonates chelates. There are also other examples of emission intensity increase under light irradiation (above 420 nm) in Eu³⁺ complexes,[36] but through a photochromic mechanism.

To simultaneously overcome the photodegradation upon UV exposure and to improve the thermal stability, mechanical features and light-emission properties (e.g., quantum yield, lifetime, photostability), Ln³⁺ complexes have been incorporated into polymers,[24,25,37,38] liquid crystals,[39] ionic liquids,[21] organic−inorganic hybrid materials,[22,23,32,40−44] zeolite L,[45] mesoporous materials,[31,34] silica nanoparticles,[27,46] and multi-walled carbon nanotubes.[47] In most of these examples, the matrix plays the role of a protective cage for the complex, strongly decreasing the UV degradation rate and could be employed in new UV dosimeters sensitive to specific wavelengths because the host absorption wavelength range may be chemically tuned. A quite interesting optical switching was reported by Yan et al. for the [Eu(dbm)₃phen] (dbm⁻ is 1,3-diphenyl-1,3-propanedionate) complex embedded in azobenzene-containing copolymers under cyclical UV (365 nm)/ visible (435 nm) light irradiation.[38] The emission intensity of the azobenzene-containing copolymers is modulated by irradiation with UV and visible light because of the reversible trans-to-cis photoisomerization reaction of the azobenzene moiety.

Cis-to-trans isomerization around double bonds, particularly C=C,[48] can be effected by direct or (mostly triplet) sensitized excitation converting, for instance, light into mechanical motion at the molecular level. In the last two decades it has been shown that the proper description of these processes requires, at least, two reaction coordinates that leads to conical intersections in the potential energy surface instead of the usual avoided crossings in the one-dimension model.[49−51] In addition, dynamic effects might be relevant[52,53] and have to be taken into consideration for a quantitative description of the isomer

selectivity, for instance. These reaction coordinates are usually associated with the torsion, the stretch and the pyramidalization of the double bonded carbon atoms in order to reach the minimal energy conical intersection. The pathway through the lowest-lying triplet state via intersystem crossing or sensitization is usually more efficient and also involves a (near) perpendicular structure of the torsion around the double bond and some degree of stretching and pyramidalization. The efficiency of this pathway is rationalized in terms of the longer lifetime of the triplet states, their lower energies, and the larger molar absorptivity of the sensitizers. When both cis and trans isomers absorb radiation or are sensitized a photostationary state is achieved (as in the examples discussed here), and at this state the rates of formation and disappearance are equal for each specie. The ratio of cis to trans isomers (photostationary mixture) depends on the relative absorption of the isomeric alkenes (for direct excitation) or, interestingly, on the sensitizer employed, specifically on the relation between the energy levels of the olefin and the triplet state of the sensitizer.[54] Particularly important to the examples addressed in this paper is the photoisomerization of stilbene that involves a twisted singlet or triplet state that can be attained from either the Z- or the E-isomer.[51] Direct irradiation (HOMO → LUMO transition) leads to isomerization via singlet state intermediates and its temperature dependence indicates that the process of formation of the twisted state from the lowest-lying singlet excited state involves small activation energy. Alternatively, the isomerization of stilbene can be attained by photosensitization, where the composition of the photostationary state strongly depends on the triplet energy of the sensitizer. For instance, the Z/E ratios in the photostationary state can vary from 1.2 up to 8.3 upon the choice of the sensitizer.[51]

Here we report that the light emission intensities of Eu³⁺ and Gd³⁺ β-diketonate complexes with photoactive t-bpete ligand (and, for the Eu³⁺ complex, also the emission quantum yield value) are significantly intensified by at least 1 order of magnitude upon UV exposure. Structural, vibrational, photophysical, and theoretical investigations were undertaken to probe the existence, in the solid state and in solution, of a trans-to-cis photoisomerization process around the −CH=CH− double bond of the photoactive t-bpete moiety leading to a photostationary state, as well as to determine its subsequent influence on the photophysical properties of the complexes. Such unprecedented improved photostability opens, for the first time, the possibility of designing and developing commercial long-term photonic devices based on Ln³⁺ β-diketonate complexes.

■ EXPERIMENTAL SECTION

Materials. The chemicals lanthanide chloride hexahydrate (EuCl₃·6H₂O and GdCl₃·6H₂O, 99.9%, Aldrich), 4,4,4-trifluoro-1-phenyl-1,3-butanedione (Hbtfa, 99%, Aldrich), trans-1,2-bis(4-pyridyl)ethylene (t-bpete, 97%, Aldrich), ethanol (EtOH, 99.9%, Merck), methanol (MeOH, 99.8%, Merck), and sodium hydroxide (NaOH, 98%, Merck) were used without further purification.

Synthesis of [Ln(btfa)₃(t-bpete)(MeOH)] (Ln = Eu, Gd) Complexes (t-Eu and t-Gd). The precursor [Ln(btfa)₃·2H₂O] (Ln = Eu and Gd) complexes (**1Eu** and **1Gd**) were prepared by the addition of 0.1 mmol of LnCl₃·6H₂O (Ln = Eu and Gd) and 0.3 mmol of btfa in 1 mL of EtOH. Then, the pH of the solution was adjusted to 6.5 with an ethanolic solution of NaOH. The resulting mixture was stirred for 24 h at room temperature and then the solvent was slowly evaporated during additional 48 h. The compound formed was washed with water and recrystallized in EtOH and dried at 45 °C during 48 h

under vacuum. To obtain *t*-Eu and *t*-Gd 0.2 mmol of *t*-bpete was added to a solution of 0.2 mmol of **1Eu** and **1Gd** in methanol. The complexes were synthesized under stirring during 24 h at room temperature. Later, the solvent was slowly evaporated at the same temperature and the compound formed was recrystallized from methanol. The obtained crystals were dried at 45 °C during 48 h under vacuum.

Anal. Calcd for $C_{43}H_{32}EuF_9N_2O_7$: C 51.00, H 3.16, N 2.77%; found C 50.60, H 3.03, N 2.80%. FT-IR (KBr): ν = 3414, 3066, 1639, 1612, 1536, 1489, 1428, 1076, 631 cm^{-1}. Anal. Calcd for $C_{43}H_{32}GdF_9N_2O_7$: C 50.74, H 3.15, N 2.75%; found C 50.82, H 3.15, N 2.74%. FT-IR (KBr): ν = 3420, 3065, 1640, 1613, 1537, 1489, 1428, 1076, 631 cm^{-1}.

Chloroform solutions (10^{-5}–10^{-2} mol·L^{-1}) of btfa and *t*-bpete ligands, **1Eu**, *t*-Eu, and *t*-Gd were also prepared for UV/vis absorption, FT-Raman, luminescence, and photostability measurements.

Powder X-ray Diffraction (XRD). Routine powder XRD data were collected at ambient temperature on a X'Pert MPD Philips diffractometer (Cu K$_{\alpha1,2}$ X-radiation, λ_1 = 1.540598 Å, λ_2 = 1.544426 Å), equipped with an X'Celerator detector and a flat-plate sample holder in a Bragg−Brentano para-focusing optics configuration (45 kV, 40 mA). Intensity data were collected by the step-counting method (step 0.02°), in continuous mode, in the $3.500 \leq 2\theta \leq 60.00°$ range.

Single-Crystal XRD. A suitable *t*-Eu single-crystal was manually harvested from the crystallization vial and mounted on a Hampton Research CryoLoop using FOMBLIN Y perfluoropolyether vacuum oil (LVAC 140/13) purchased from Sigma-Aldrich,[55] with the help of a Stemi 2000 stereomicroscope equipped with Carl Zeiss lenses. Data were collected at 150(2) K on a Bruker X8 Kappa APEX II charge-coupled device area-detector diffractometer (Mo K$_\alpha$ graphite-monochromated radiation, λ = 0.71073 Å) controlled by the APEX2 software package[56] and equipped with an Oxford Cryosystems Series 700 cryostream monitored remotely using the software interface Cryopad.[57] Images were processed using the software package SAINT+,[58] and data were corrected for absorption by the multiscan semiempirical method implemented in SADABS.[59] The crystal structure was solved by employing the Patterson algorithm implemented in the software package SHELXS-97.[60,61] This approach allowed the immediate location of the Eu^{3+} metallic center. All remaining non-hydrogen atoms were directly located from difference Fourier maps calculated from successive full-matrix least-squares refinement cycles on F^2 using SHELXL-97.[61,62]

Even though the vast majority of the non-hydrogen atoms could be refined using anisotropic displacement parameters, the extensive structural disorder arising from thermal vibration of the terminal −CF$_3$ groups and the coordinated methanol molecule prevented a priori an identical treatment for the atoms associated with one −CF$_3$ moiety (namely, carbon C22) and of the pendant −CH$_3$ group. These atoms (C and F) were instead included in the final structural model using independent isotropic displacement parameters. All −CF$_3$ groups were also refined with the C−F and F···F distances restrained to 1.33(1) and 2.10(1) Å, respectively, to ensure a chemically reasonable environment for these moieties. In addition, within the coordinated methanol molecule, the C−O distance was also restrained to 1.44(1) Å to avoid divergence of the overall structural refinement.

Hydrogen atoms bound to carbon were placed at idealized positions using appropriate *HFIX* instructions in SHELXL: 43 for the aromatic carbons and 33 for the carbon atom associated with the coordinated methanol molecule. All these atoms have been included in subsequent refinement cycles in riding-motion approximation with U_{iso} fixed at 1.2 (for the former groups) or $1.5 \times U_{eq}$ (only for the −CH$_3$ moiety) of the carbon atom to which they are attached, respectively.

Noteworthy, the crystal structure of compound *t*-Eu exhibits a number of limitations mainly because of the systematic poor quality of the available crystals. Collection of a better data set seems to be only possible if better crystals are isolated using most likely a synchrotron source. Nevertheless, it is important to note that the structural model derived from the collected data set clearly supports and is further corroborated by the information derived from other techniques that were employed throughout the manuscript.

The last difference Fourier map synthesis showed the highest peak (2.436 e Å^{-3}) and deepest hole (−1.803 e Å^{-3}) located at 0.98 and 0.88 Å from Eu1, respectively.

Crystallographic data collection and structure refinement details are summarized in Table 1. Selected bond lengths and angles for the Eu^{3+}

**Table 1. Crystal and Structure Refinement Data of *t*-Eu**

formula	$C_{43}H_{32}EuF_9N_2O_7$
formula weight	1011.67
crystal system	monoclinic
space group	$P2_1/n$
a (Å)	13.2740(9)
b (Å)	20.7777(13)
c (Å)	15.4274(10)
β (deg)	94.333(3)
volume (Å^3)	4242.8(5)
Z	4
D_c (g cm^{-3})	1.584
μ(Mo Kα) (mm^{-1})	1.569
crystal size (mm)	0.20 × 0.12 × 0.03
crystal type	colorless block
θ range	3.53–25.34
index ranges	$-15 \leq h \leq 15$
	$-24 \leq k \leq 24$
	$-18 \leq l \leq 18$
reflns collected	32 621
independent reflns	7680 [R_{int} = 0.0812]
completeness to θ = 25.34°	98.9%
final R indices [$I > 2\sigma(I)$]^{a,b}	R1 = 0.1065
	wR2 = 0.2730
final R indices (all data)^{a,b}	R1 = 0.1951
	wR2 = 0.3405
weighting scheme^c	m = 0.1393
	n = 59.9945
largest diff. peak and hole	2.436 and −1.803 eÅ^{-3}

^{a}R1=$\sum\lVert F_o\rvert - \lvert F_c\rVert/\sum\lvert F_o\rvert$. ^{b}wR2 = $\left(\sum[w(F_o^2 - F_c^2)^2]/\sum[w(F_o^2)^2]\right)^{1/2}$. ^{c}w = $1/[\sigma^2(F_o^2) + (mP)^2 + nP]$, where $P = (F_o^2 + 2F_c^2)/3$.

coordination environment and hydrogen bonding geometry are presented in Tables S1 and S2, respectively, in the Supporting Information. Structural crystallographic drawings have been produced using the software package Crystal Diamond.[63]

Crystallographic data (including structure factors) have been deposited with the Cambridge Crystallographic Data Centre as supplementary publication no. CCDC-905544. Copies of the data can be obtained free of charge on application to CCDC, 12 Union Road, Cambridge CB2 2EZ, U.K. Fax: (+44) 1223 336033. E-mail: deposit@ccdc.cam.ac.uk.

Analysis, Spectroscopy, and Photophysics. Elemental analyses for C, H, and N were performed with a CHNS-932 elemental analyzer using standard combustion conditions and handling of the samples in air. Mid-infrared spectra (FT-IR) were recorded using a MATTSON 7000 FTIR spectrometer. The spectra were collected over the range 4000−250 cm^{-1} by averaging 128 scans at a maximum resolution of 2 cm^{-1}. The compounds were finely grounded (about 2 mg), mixed with approximately 175 mg of dried KBr (Merck, spectroscopic grade), and pressed into pellets. Attenuated total reflectance (ATR) FT-IR spectra were measured on the same instrument equipped with a Specac Golden Gate Mk II ATR accessory having a diamond top-plate and KRS-5 focusing lenses. The FT-Raman spectra were recorded on a FT Bruker RFS-100 spectrometer using a Nd:YAG laser (Coherent Compass-1064/500N) with excitation wavelength of 1064 nm and a resolution of 2 cm^{-1}. The UV/vis absorption and diffuse reflectance spectra were recorded on a JASCO V-560 instrument over the scan range 220−850 nm, at 200 nm min^{-1} and a resolution of 0.5 nm. The luminescence spectra were recorded with a modular double grating
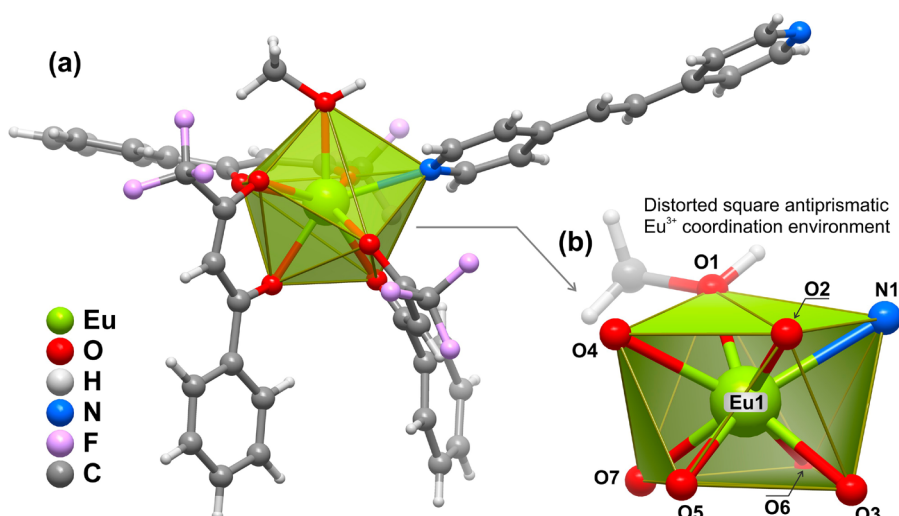
Figure 1. (a) Mixed ball-and-stick and polyhedral representation of the molecular unit composing the crystal structure of *t*-Eu. (b) Detailed view of the distorted square antiprismatic coordination environment of the crystallographic independent Eu^{3+} metallic center present in *t*-Eu. For selected bond lengths and angles for the {$EuNO_7$} coordination environment see Supporting Information Table S1.

excitation spectrofluorimeter with a TRIAX 320 emission mono-chromator (Fluorolog-3, Horiba Scientific) coupled to a R928 Hamamatsu photomultiplier, using the front face acquisition mode. The excitation source was a 450 W Xe arc lamp. The emission spectra were corrected for detection and optical spectral response of the spectrofluorimeter and the excitation spectra were corrected for the spectral distribution of the lamp intensity using a photodiode reference detector. The emission decay curves were acquired with the same instrumentation, using a pulsed Xe−Hg lamp (6 μs pulse at half-width and 20−30 μs tail). The photostability experiments were performed on the same setup employed to measure the luminescence spectra. The selected irradiation wavelengths were 280, 330, and 360 nm for a maximum exposure time of 10 h. The irradiation power of the 450 W Xe arc lamp was quantified using a power meter (Coherent, Field MaxII-TOP) coupled to a high-sensitivity silicon photodiode optical sensor (diameter of 7×10^{-3} m, Coherent, OP-2 VIS), yielding irradiance values of 78, 99, and 105 W m^{-2}, respectively. The emission quantum yields (ϕ) were measured using the C9920-02 measurement system from Hamamatsu with a 150 W Xe lamp coupled to a monochromator for wavelength discrimination, an integration sphere as sample chamber and a multichannel analyzer for signal detection. Three measurements were made for each sample and the average values obtained are reported with accuracy within 10% according to the manufacturer. Apart some luminescence spectra recorded at 11 K, all the other measurements were performed at room temperature.
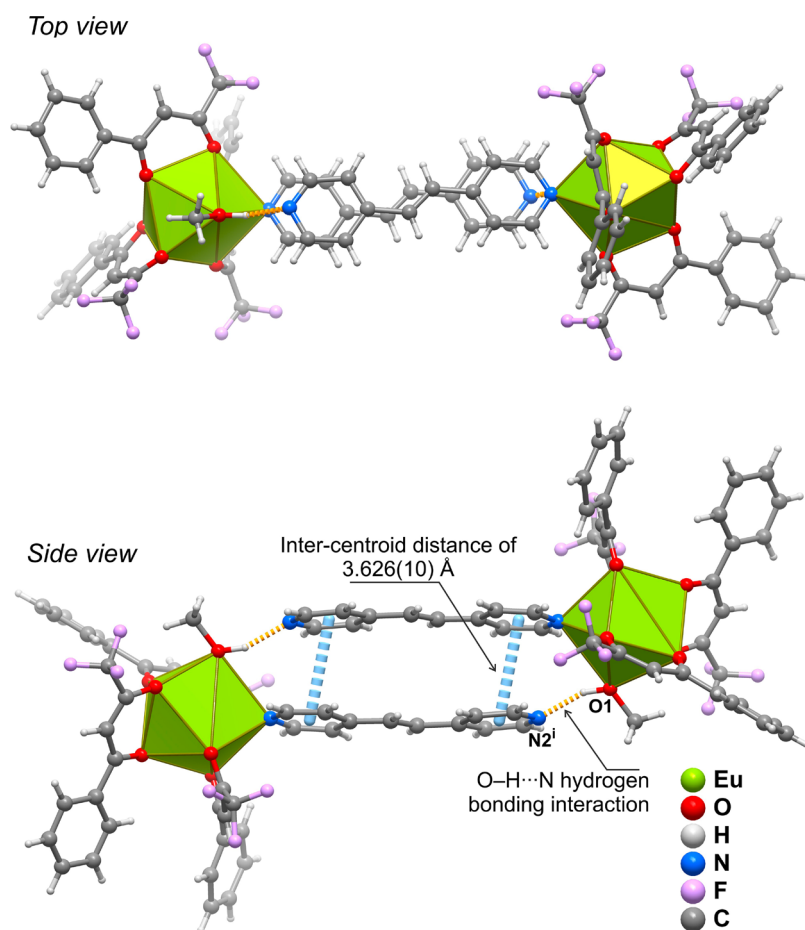
Computational Details. Recent investigations have shown that the B3LYP functional is reliable for describing the geometrical parameters and electronic structure of lanthanide complexes even when the 4f electrons are included in the core.[64−69] Thus, we employed the MWB52[70] effective core potential including the 4f^6 electrons to describe the Eu^{3+} ion for calculations of the structures and ligand-based properties. Standard 3-21G basis sets were employed for the H, C, N, and F and 6-31+G for O atoms. With this approach, the Eu^{3+} ion becomes closed-shell, so the complexes have an even number of electrons leading to a singlet ground-state (S_0) and the lowest-lying excited state is a triplet (T_1). The molecular structures of *t*-Eu and of the [Eu(btfa)$_3$(*c*-bpete)(MeOH)] complex (*c*-Eu) with the bpete ligand in the trans and cis stereochemistry, respectively, were fully optimized in their S_0 and T_1 states, in the gas-phase and without symmetry constraints. Harmonic vibrational frequencies were calculated at the same level for all optimized structures, which were shown to have no negative force constants. The lowest triplet state was investigated with the spin-unrestricted method (UB3LYP). Calculated expectation values for the total spin operator, $\langle S^2 \rangle$, prior to spin annihilation are 2.0524 and 2.0110 for the triplet state structures *t*-Eu

and *c*-Eu, respectively, and become 2.0017 and 2.0001 after annihilation of the first spin contamination, sufficiently close to the expected $\langle S^2 \rangle$ = 2 for triplet states. Using the optimized ground-state structure of *t*-Eu, the vertical electronic excitation energies related to the absorption in solution were obtained by time-dependent DFT (TD-DFT) calculations[71] with the B3LYP functional and included the solvent effects via the polarizable continuum model (PCM).[72] The solvent used in the PCM calculations was chloroform and the united atom topological model radii were employed to generate the solute cavity within the PCM implementation. Adiabatic transition wave-numbers (for the triplet state of *t*-Eu and *c*-Eu) were calculated within the framework of the so-called ΔSCF procedure. All the quantum chemistry calculations were performed with Gaussian 03W, revision D.02 program[73] using its default criteria.

RESULTS AND DISCUSSION

First, we will recall the structural and electronic properties of *t*-Eu and *t*-Gd. The results are presented and discussed in two sections: i) description of the crystal structures together with DFT calculations to provide structural information of the ground-state S_0 geometries; ii) photophysical characterization (UV/vis and photoluminescence spectroscopy) together with TD-DFT calculations to describe the excited singlet and triplet states. Then, we will focus on the impact of UV light irradiation with different wavelengths on the spectroscopic and photo-physical properties. Its influence on the crystal structure, vibrational and electronic properties as well as on the photoluminescence, emission quantum yield, ligands-to-metal charge transfer (LMCT) bands and photostability features are presented and discussed together with theoretical results obtained for both *t*-Eu and *c*-Eu complexes at S_0 and T_1 geometries.

Single-Crystal and Powder XRD, DFT Calculations. *t*-Eu crystallizes in the centrosymmetric monoclinic $P2_1/n$ space group (Table 1) and its crystal structure determined at 150 K reveals a whole molecule composing the asymmetric unit as depicted in Figure 1a. As described in the dedicated technical section, the crystal itself (the best diffracting from a handful of batches) presented some problems, mainly associated with structural disorder attributed to thermal vibrations. Never-theless, it is important to stress that the crystallographic features highlighted in the following paragraphs, and which

Top view

Side view

Inter-centroid distance of
3.626(10) Å

O1

N2ⁱ

O−H···N hydrogen
bonding interaction

🟢	**Eu**
🔴	**O**
⚪	**H**
🔵	**N**
🟣	**F**
⚫	**C**

Figure 2. Perspective views of the supramolecular dimers present in the crystal structure of *t*-**Eu** formed by the combined effect of strong and highly directional O−H···N hydrogen bonds (connecting *t*-bpete units to methanol molecules) and π−π supramolecular contacts (between adjacent *t*-bpete molecules). For geometrical details on the represented hydrogen bonds see Supporting Information Table S2.

constituted the basis for the DFT calculations, were unequivocally determined being representative of the whole bulk material. Even though *t*-**Gd** could not be isolated as single-crystals suitable for the same type of studies, powder XRD studies on the bulk materials (Figure S1 in the Supporting Information) clearly show that the two compounds are isotypical.

The crystal structure of *t*-**Eu** is composed of a single crystallographically independent Eu³⁺ cation which is coordinated to three *O,O*-chelated btfa⁻ anionic ligands, one methanol molecule and one *t*-bpete linker bound by a single nitrogen atom. The overall {EuNO₇} coordination environment can this be envisaged as a highly distorted square antiprism (Figure 1b) in which both the methanol and the *t*-bpete linker are cis in the same basal plane (O1 → N1 → O2 → O4): even though the Eu−(N,O) distances range fall in the relatively narrow 2.326(11)−2.599(12) Å range (the longest connection is observed for the Eu−N linkage to bpete), the internal cis and trans polyhedral angles are significantly more spread as depicted in Table S1 in the Supporting Information (Figure 1b for the atomic labeling). As a consequence, the two average basal planes (O1 → N1 → O2 → O4 and O3 → O5 → O7 → O6) are also not exactly parallel subtending a mutual ~6.7° angle.

Both the methanol and the *t*-bpete linker play an important supramolecular role in the crystal packing of *t*-**Eu**. As shown in Figure 2, the coordinated −OH group of methanol donates the

hydrogen atom in a hydrogen bonding interaction to the uncoordinated pyridyl group of the neighboring *t*-**Eu** complex (Table S2 in the Supporting Information for geometrical details on the hydrogen bonds). As this process is structurally concerted, a supramolecular dimer is formed whose structural robustness is further incremented by the presence of offset π−π contacts between the adjacent pyridil groups.

Concerning the structural properties, the crystallographic data of *t*-**Eu** was used as a starting point for the B3LYP geometry optimizations of the monomeric structures. The optimized structure for *t*-**Eu** (Figure S2a in the Supporting Information) was compared directly with the crystallographic structure and was employed to simulate the properties of the complex in solution. The agreement between the calculated bond lengths of Eu−O and Eu−N and the experimental data is quite satisfactory, with the largest difference being 0.08 Å for the Eu−O1 bond, an average unsigned mean error of only 0.04 Å for the coordination polyhedron, and errors in the bond angles smaller than 3°. The overall calculated structure is in remarkable agreement with the crystallographic one despite of the following simplification of the calculated model, namely, only the monomer is employed and different basis sets are used for oxygen and the remaining atoms. The structure of the complex containing the *cis*-isomer, *c*-**Eu**, was also calculated at the same level of theory (Figure S2b in the Supporting Information) and compared with the *t*-**Eu** structure. The calculated values for Eu−O and Eu−N bond distances decrease

(a)

(b)
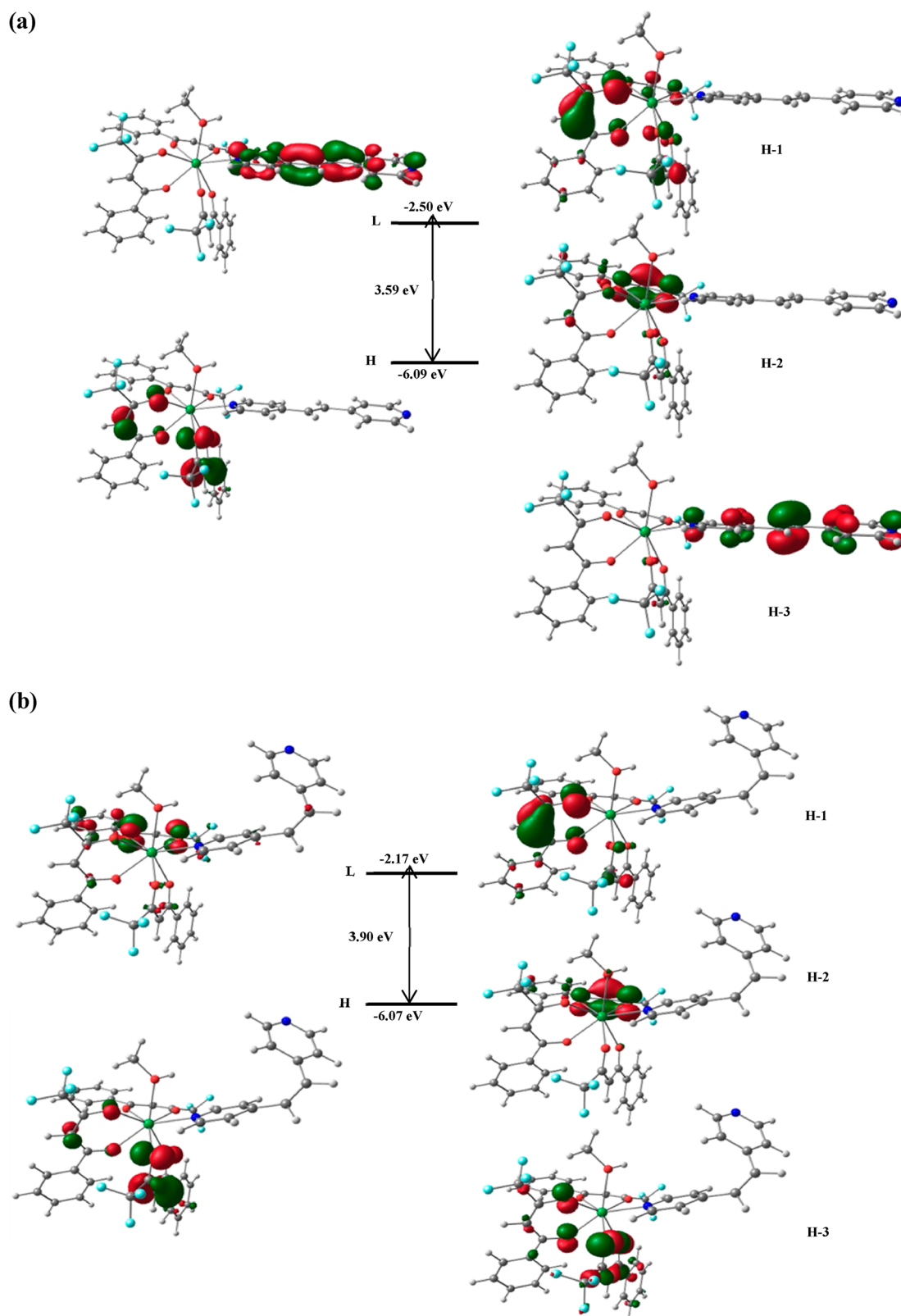
Figure 3. Schematic diagram showing the electronic density contours for the HOMO (H), H − 3, H − 2, H − 1, and LUMO (L) molecular orbitals of (a) *t*-Eu and (b)*c*-Eu.

by 0.003−0.011 and 0.038 Å, respectively, from the calculated values for *t*-Eu structure and the whole unit of bpete is modified. As the C═C bond is rotated by 4.1° to decrease the H···H steric repulsions between the pyridyl rings, the *c*-bpete isomer is nonplanar. Additionally, some changes in the bond lengths in the vinyl region are also observed. The C═C distance is slightly shortened from 1.346 to 1.344 Å and the neighboring C−C bonds are lengthened by 0.01 Å.

UV/vis Absorption and TD-DFT calculations. In order to provide the framework for the excited state TD-DFT results, it will be useful to examine the electronic structure in terms of the HOMO (H) and LUMO (L) molecular orbitals for both *t*-**Eu** and *c*-**Eu** isomers (Tables S3a,b in the Supporting Information). The partial molecular orbital compositions (H − 16 through L + 6, in vacuum and in CHCl$_3$ solvent) relevant to the interpretation of the UV/vis absorption results are listed in Table S3a in the Supporting Information and in Figure 3 (that displays the electronic character of the H − 3, H − 2, H − 1, H, and L orbitals for the *t*-**Eu** monomer. The H − 2, H − 1, and H orbitals are mainly composed of the btfa π orbitals while the L is localized on the *t*-bpete ligand. The H − 3 orbital involves a mixture of 72% btfa and 23% *t*-bpete orbitals (Table S3a in the Supporting Information). The calculated optical energy gap, 3.59 eV (345 nm), is close to the lowest energy absorption edge of the UV/vis absorption spectrum (Figure 4,
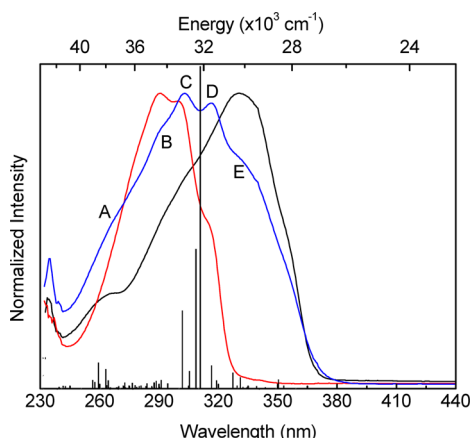
Figure 4. UV/vis absorption spectra of btfa (black line), *t*-bpete (red line) and *t*-**Eu** (blue line). The vertical lines correspond to the calculated transitions (TD-DFT) for *t*-**Eu**.

~385 nm) and is within the reported values for most of Eu^{3+} complexes.[68,74,75] The UV/vis absorption spectra of *t*-bpete, btfa and *t*-**Eu** in chloroform solutions (1.4 × 10^{-5} mol·L^{-1}) exhibit broad bands (240−380 nm) with high molar absorption coefficients characteristic of singlet intraligand (^{1}IL) π→π* transitions and main components peaking at ~260, 290, 300, 315, and 340 nm (Figure 4).

The corresponding TD-DFT singlet electronic transitions (containing the solvent, chloroform, effects) are included in Figure 4 and the calculated singlet−singlet energies, oscillator strengths, and the molecular orbitals mainly involved in the selected transitions are listed in Table S4 in the Supporting Information. Given the complexity of the system and to make a reliable assignment of the molecular orbitals involved in the excitation of each dominant absorption observed in the experimental spectrum, singlet states were also calculated for the optimized structure of the **1Eu** complex.

According to the DFT and TD-DFT results (Tables S3 and S4 in the Supporting Information), the *t*-bpete ligand shows characteristic intraligand ^{1}IL π→π*$_{t\text{-bpete}}$ transitions at 290, 300, and 315 nm, where the latter is red-shifted to E (340 nm), while the former transitions remained practically unaltered, B (291 nm) and C (303 nm), upon complexation. In addition, the absorption bands labeled as A (260 nm) and D (316 nm) are assigned to excitations predominantly involving ^{1}IL π→

π*$_{btfa}$ transitions although with some minor contributions from the *t*-bpete ligand. The lowest-energy absorption band in the 325−385 nm region (denoted as E in Figure 4 and in Table S4 in the Supporting Information) receives a great contribution of the 315 nm red-shifted transition of the photoisomerizable *t*-bpete ligand upon coordination, similarly to shifts observed after the *t*-bpete protonation.[76] Therefore, it is expected that excitation in this region where the *t*-bpete effectively absorbs may enhance the population of ^{3}IL$_{t\text{-bpete}}$ by the intersystem crossing (ISC) from the ^{1}IL$_{t\text{-bpete}}$ because of coordination to Ln^{3+} ions, and consequently to an efficient trans-to-cis photoisomerization process.[76,77] The occurrence of a triplet mechanism for the isomerization of free *t*-bpete ligand is well established[78] and, for the Ln^{3+} complexes, as the triplet pathway becomes more competitive than the singlet, because of the heavy atom effect, the ^{3}IL$_{t\text{-bpete}}$ state should be the main pathway for the photoisomerization.[79−81]

Interestingly, the trans-to-cis photoisomerization of bpete ligand induced by UV irradiation has been demonstrated to be responsible for the emission intensity increase observed in solutions of rhenium complexes.[76,80,82,83] Whereas among these examples those containing the *c*-bpete ligand exhibit luminescence after UV irradiation, no emission has been reported at all for complexes containing the *t*-bpete counterpart. These and the foregoing results lead us to evaluate the possibility of a trans-to-cis photoisomerization occurrence in *t*-**Eu** and *t*-**Gd**. To validate this hypothesis, a chloroform solution (1.4 × 10^{-5} mol·L^{-1}) of *t*-**Eu** was investigated by UV/vis absorption after 3 h under irradiation at 360 nm. It should, however, be noted that the time required for the data acquisition can slightly change the profile of the UV/vis absorption spectrum before irradiation. Different spectral patterns in the UV/vis absorption spectra before and after irradiation were observed and overall an unexpected increase of the molar absorption coefficient was noted (Figures S3a,b in the Supporting Information). The spectral changes between 280 and 380 nm suggest a simultaneous increase of btfa absorption and an absorption decrease of the bpete ligand. To reliably compare the spectral changes, the UV/vis absorption spectra were normalized at 316 nm (^{1}IL π → π*$_{btfa}$ transition). After irradiation and according to the TD-DFT calculations, a decrease in the relative intensity of the components attributed to the bpete ligand, 291 and 303 nm, was noted. Nevertheless, an increase in the components at 260 and 340 nm (predominantly involving btfa with minor contributions from bpete) was observed (Figure S3a in the Supporting Information). In addition to intensity changes, small red-shifts in the absorption components at 260−265 and 316−318 nm were also discerned. The band at ~260 nm showed only a small increase in intensity when a chloroform solution of **1Eu** (1.4 × 10^{-5} mol·L^{-1}) was irradiated in the same conditions (Figure S4 in the Supporting Information), however there was no detected shift in its position. According to the literature,[84] the absorbance of 84% *c*-bpete is negligible in the region between 300 and 325 nm and the UV/vis absorption spectrum also displays a component around 240 nm, which is absent in the *t*-bpete absorption spectrum.[85] A similar behavior was also observed for rhenium complexes with coordinated bpete ligand.[77,83,85] For example, it was found[83] that irradiation at 350 nm of a degassed CH$_2$Cl$_2$ solution of [Re(Me$_2$bpy)-(CO)$_3$(*t*-bpete)PF$_6$] (with Me$_2$bpy being 4,4′-dimethyl-2,2′-bipyridine) leads to a intensity absorption decrease below 270 nm, while an increase was observed between 270 and 222 nm.

It is therefore clear from the previous considerations that, in our results, the arising of the component around 265 nm and the observed intensity decrease of the components at 291 and 303 nm support the existence of a trans-to-cis photoisomerization process in *t*-Eu and *t*-Gd.

In addition to the previous TD-DFT studies of singlet-excited states, we have examined the lowest excited triplet state of the *t*-Eu monomer by optimizing the triplet state geometry with the UB3LYP method (Figure S5 in the Supporting Information). This will provide an indication of the triplet emission energy and geometry relaxation that occurs in the excited state in possible emission processes. The ΔSCF approach was applied and upon geometry relaxation in the T_1 state an excitation energy of 22222 cm^{-1} was predicted, in very good agreement with the experimental value of 22480 cm^{-1} measured from the emission spectrum of *t*-Gd at 11 K (Figure S6 in the Supporting Information). Considering the nature of the H and L frontier orbitals, it is observed that the H is localized on the *t*-bpete ligand while the L mainly involves the btfa π^* orbitals. When exciting the singlet ground state of *t*-Eu to the lowest-lying triplet state, a structural reorganization of the *t*-bpete ligand is observed and involves a change from a trans stereochemistry in the S_0 state (Figure S2a in the Supporting Information) to a nearly perpendicular orientation between the pyridyl rings (Figure S5 in the Supporting Information) in the T_1 state. According to Dattelbaum et al. (transient IR measurements),[80] a perpendicular T_1 configuration was proposed as the immediate precursor to the trans-to-cis conversion.

Therefore, and according to our results, a triplet mechanism involving an ISC process followed by isomerization along a triplet potential energy surface that nearly crosses with the ground singlet surface near 90° is expected. The molecule can then either rotate further 90° to the cis isomer or twist back to the trans configuration. The ΔSCF approach was also applied to the *c*-Eu monomer. A decrease of the emission energy is predictable with a trans-to-cis process, which is in agreement with the experimental results. However, the calculated T_1 excitation energy of 19763 cm^{-1} is underestimated compared to the experimental 21728 cm^{-1} value (Figure S6 in the Supporting Information).

The photostability study performed in solid state, mainly the UV irradiation influence on the ligands, was also monitored through diffuse reflectance of *t*-Eu and *t*-Gd (Figure 5). The UV irradiation at 360 nm induces red-shifts and changes in the intensities of the components around 265 and 320 nm. As a consequence of these red-shifts, the color of the samples was changed from light to dark yellow reinforcing the occurrence of a trans-to-cis transformation.

Raman Spectroscopy. Further evidence of the occurrence of a trans-to-cis photoisomerization of the bpete moiety was found by Raman spectroscopy of the *t*-Eu chloroform solutions before and after irradiation at 360 nm (Figure S7a-c in the Supporting Information). To enhance the Raman signal, concentrated solutions (1.0×10^{-2} mol·L^{-1}) were prepared and irradiated. Additionally, to be sure that the analysis of the vibrational modes affected by this transformation were specifically attributed to the bpete ligand, Raman spectra of solid samples of **1Eu**, *t*-bpete ligand and *t*-Eu were also recorded (Figure S8a-c in the Supporting Information). The bands at 1010 cm^{-1} (pyridyl ring breathing), 1609 cm^{-1} (CC/CN stretching modes of pyridyl ring) and 1641 cm^{-1} (ethylenic C═C stretching) in the spectrum of the *t*-bpete ligand are used
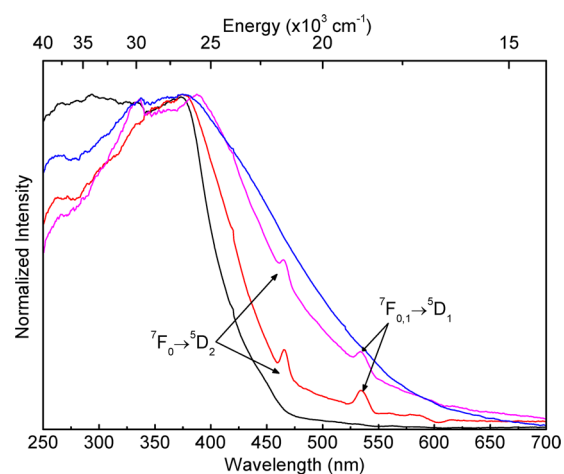

Figure 5. Diffuse reflectance spectra of *t*-Eu (red) and *t*-Gd (black). The corresponding spectra acquired after irradiation at 360 nm during 10 h are also shown (magenta, *t*-Eu, and blue, *t*-Gd).

to assign the bands at 994, 1595, and 1638 cm^{-1} in the spectrum of *t*-Eu, which are red-shifted due to the coordination. However, it is important to note that the sample containing the *t*-bpete ligand is not completely pure as evidenced by the presence of a band at 1632 cm^{-1} characteristic of the *cis*-bpete C═C stretching vibration. Upon irradiation (Figure S7a-c in the Supporting Information) it is observed that the Raman intensities of the bands in chloroform solutions at 1607 cm^{-1} and 1011 cm^{-1} (in correspondence with the bands at 1609 and 1010 cm^{-1} in the solid state) are significantly reduced, whereas the opposite behavior is observed for the component at 1632 cm^{-1}. As the bpete sample contains *cis* and *trans* forms, residual *c*-bpete can be found in *t*-Eu before irradiation. In fact, the *cis*-component at 1632 cm^{-1} is already noted in the spectrum of the solution before irradiation, thus verifying its enhancement with irradiation. Additionally, there is no disappearance of the band at 1639 cm^{-1} characteristic of the *t*-bpete C═C stretching vibration, suggesting that an equilibrium between the two isomers is achieved upon irradiation. This is consistent with a *photostationary state* commonly observed in trans-to-cis photoisomerization when both isomeric forms are excited or sensitized. According to the B3LYP calculated frequencies and intensities, which are in complete agreement with the experimental results (Tables S5, S6 in the Supporting Information), a significant decrease of the Raman intensity is expected for both ring breathing and CC/CN stretching modes of pyridyl ring with a trans-to-cis transformation. Additionally, a calculated ethylenic C═C stretching blue-shift from 1626 to 1618 cm^{-1} is also expected.

In summary, the remarkable gain in intensity observed in the UV/vis absorption spectra and the existence of characteristic frequencies of the *cis*-isomer identified by Raman spectroscopy, demonstrates the formation of *c*-Eu and thus the occurrence of a trans-to-cis photoisomerization process in the solid state. In this context, the results presented hereinafter will be discussed based on this process.

Photoluminescence Spectroscopy. The room-temperature emission features of one *t*-Eu single crystal were studied under direct intra-4f^6 excitation ($^5D_2$, 464 nm), Figure 6a. The emission spectrum reveals a single component for the nondegenerate $^5D_0 \rightarrow {}^7F_0$ transition (Figure 6b) and a J-degeneracy splitting of the $^7F_{1,2}$ levels into 3 and 5 Stark
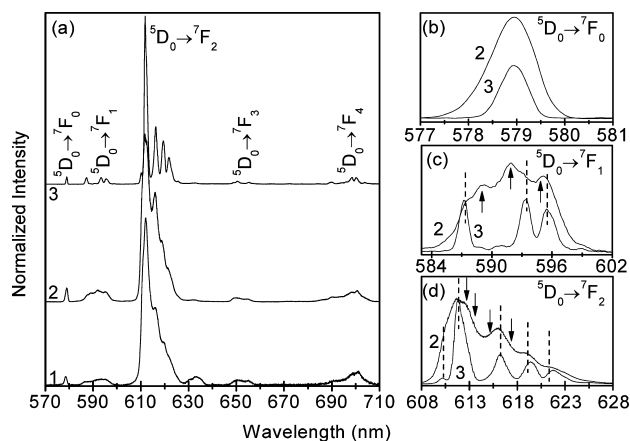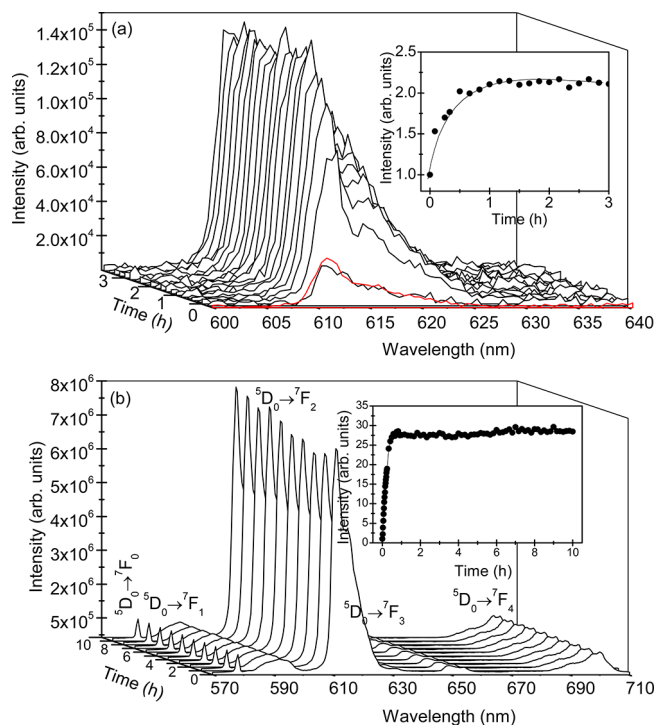
Figure 6. (a) Emission spectra of one *t*-Eu single crystal acquired at (1) 300 K, excited at 464 nm, and of an ensemble of *t*-Eu single crystals at 11 K, excited at (2) 360 and (3) 464 nm. (b–d) Magnification of the $^5D_0 \rightarrow ^7F_{0-2}$ transitions, respectively, measured at 11 K and excited at (2) 360 and (3) 464 nm.

components (marked with vertical lines in Figures 6c,d), respectively, indicating that the Eu^{3+} ions occupy a low symmetry site without an inversion center (labeled as Site 1), in accordance with the higher intensity of the electric-dipole $^5D_0 \rightarrow ^7F_2$ transition and as the single crystal XRD results pointed out. Moreover, the $^5D_0$ emission decay curve monitored within the $^5D_0 \rightarrow ^7F_2$ transition and excited at 465 nm displays a single exponential behavior (Figure S9 in the Supporting Information), yielding a lifetime value of (0.261 ± 0.006) × 10^{-3} s.

Changing the excitation wavelength induces the appearance of an unusual phenomenon characterized by an intensification of the emission intensity. Figure 7a shows the dependence of the $^5D_0 \rightarrow ^7F_2$ transition integrated intensity as function of the irradiation time. The emission spectra were scanned with low integration time to minimize the effect of the irradiation during the spectra acquisition. To enhance the signal-to-noise ratio, the same experiment was carried out using an ensemble of single crystals (Figure 7b). In both cases, after 20 min of irradiation the emission is intensified over an order of magnitude being photostable under continuous UV irradiation over, at least, 10 h. This is indeed the first time that lanthanide β-diketonates chelates are photostable under UV irradiation for long-time exposure, therefore, do not presenting the typical photobleaching of these materials that has hindered their applications in photonic devices.

Aiming at obtaining further insights into this intriguing phenomenon, the emission features of *t*-Eu single crystals were investigated at 11 K, in order to maximize the emission intensity and decrease the thermal-induced broadening of the intra4f^6 transitions observed at 300 K. Figure 6a shows the emission spectra of the *t*-Eu crystals after irradiation at 360 nm for 10 h under distinct excitation wavelengths. Apart from a narrowing of the intra4f^6 lines, the spectrum excited at 464 nm resembles that acquired at 300 K prior to irradiation. Changing the excitation wavelength to 360 nm, the emission features are marked changed, being observed an increase in the relative intensity (~50%) and a broadening (~4.3%) of the $^5D_0 \rightarrow ^7F_0$ transition (Figure 6b) and changes in the number and energies of the Stark components of the $^5D_0 \rightarrow ^7F_{1,2}$ transitions (Figures 6c,d). In particular, the $^5D_0 \rightarrow ^7F_1$ transition shows 6 Stark components, in which 3 are ascribed to Site 1 and already
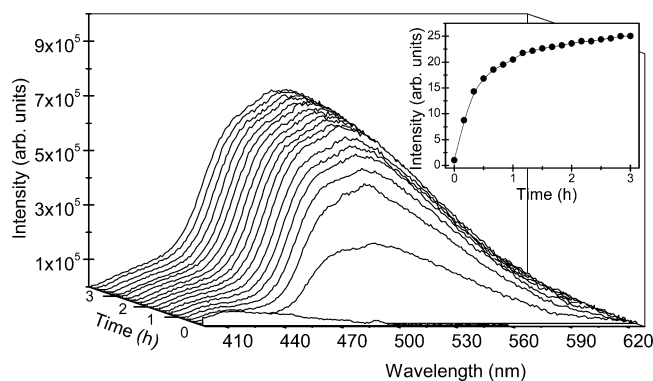

Figure 7. Emission spectra (300 K) of (a) one *t*-Eu single crystal and (b) an ensemble of *t*-Eu crystals, excited at 360 nm, as function of the irradiation time at 360 nm. The emission spectrum (acquired using the same experimental conditions) of the crystal face not previously exposed to the radiation (the single crystal was rotated by 180°) is presented in red in (a). The insets show the integrated intensity variation of the $^5D_0 \rightarrow ^7F_2$ transition with the irradiation time. The lines are visual guides.

detected under excitation at 465 nm (marked with vertical lines in Figure 6c) and 3 new Stark components (marked with arrows in Figure 6c) that unequivocally demonstrate that a new Eu^{3+}-local environment is created after UV irradiation (labeled as Site 2). Therefore, it is clear that under irradiation there is a partial alteration of the Eu^{3+}-local sites being that some of the Eu^{3+} ions remain unaltered (Site 1) and that another Eu^{3+}-local environment is created under irradiation (Site 2). These observations also suggest that a photostationary state due to cis-trans photoisomerization is established, thus generating the additional Site 2. It is well-known that cis-to-trans isomerization processes induce large mechanical motions via one-bond-flip mechanism, which is thus inhibited in solid solutions or crystals as observed for diarylethenes.[86] Thus, it is expected that mechanical and steric constraints could be present in the crystal, which hinder cis-trans photoisomerization in the bulk, suggesting that this process is confined to the surface exposed to the UV irradiation. This hypothesis was tested by recording the emission spectrum of one *t*-Eu single crystal after 180° rotation, so that the emission features were acquired from the crystal face not exposed directly to the UV irradiation. The emission spectrum reveals the same emission intensification (Figure 7a), pointing out that this phenomenon occurs at the crystal surface, due to stereochemical constraints arising from the appearance of the new Eu^{3+} environment (Site 2).

The intra4f emission intensity enhancement (Figure S10 in the Supporting Information) and the presence of two Ln^{3+}-local sites (Figure S11 in the Supporting Information) after irradiation are also detected for chloroform *t*-Eu solutions (1.4

$\times 10^{-4}$ and 1.0×10^{-2} mol·L^{-1}). Similarly to that found for the crystals, the emission-integrated intensity is increased by 1 order of magnitude.

The emission intensification is also clearly discerned for *t*-Gd in solid-state (Figure 8). The spectra show a broad band

Figure 8. Emission spectra (300 K) of one single *t*-Gd single crystal, excited at 360 nm, as function of the irradiation time at 360 nm. The inset shows the integrated intensity variation of the $S_1 \rightarrow S_0$ transition (no detected emission with 0.05×10^{-3} s delay time) with the irradiation time.

assigned to the singlet excited states of btfa and *t*-bpete ligands, whose intensity is drastically intensified over 1 order of magnitude in the first hour under irradiation, reaching its maximum constant value after 2–3 h. After, the emission intensity remains practically constant during more 7–8 h demonstrating the photostability of the complex under UV irradiation. In addition to the emission intensification, the spectrum of *t*-Gd displays a red-shift, from 440 to 515 nm, and an increase in the full-width at half-maximum (fwhm), from ~3265–4440 cm^{-1}, indicating that structural modifications on the ligands conformation is induced by UV irradiation, as detailed below. This unusual emission intensity enhancement also occurs for irradiation wavelengths between 330 and 420 nm (illustrated in Figure S12a in the Supporting Information for 330 nm).

For high irradiation energies (>30 750 cm^{-1}, wavelengths lower than 325 nm), however, after 20 min upon irradiation a decrease of the intensity was detected, which confers the typical photobleaching behavior observed in lanthanide β-diketonate complexes (Figure S12b in the Supporting Information). This is consistent with the results reported for rhenium complexes containing the *t*-bpete ligand that also undergo photodamages upon irradiation at 250 nm.[83] Therefore, in this work we will limit the irradiation energy at values lower than 30300 cm^{-1}, that is, wavelengths longer than 330 nm.

The emission intensification induced by the UV exposure has remarkable repercussions in the emission quantum yield values. Prior to irradiation, the emission quantum yield values of all the Eu^{3+}-crystal were not detectable in our experimental setup ($\phi <$ 0.01), independently of the excitation wavelength (280–465 nm). Nevertheless, after 10 h under 330 nm irradiation, it is observed an increase in the quantum yield value up to 0.29 ± 0.03 (excitation at 360 nm), so at least 30 times.

This quantum yield value variation may be rationalized in terms of the energy of the triplet and ligands-to-metal charge transfer (LMCT) states before and during irradiation (10 h). The triplet energy was estimated from the onset of the 11 K time-resolved phosphorescence spectrum of *t*-Gd (arrows in

Figure S6b in the Supporting Information). The value prior to the irradiation, 444.0 nm (22522.5 cm^{-1}) shifts toward longer wavelengths during irradiation 460.2–462.2 nm (21635.7–21729.7 cm^{-1}), as discussed below. The LMCT energy was estimated from the comparison between the diffuse reflectance of *t*-Eu and *t*-Gd shown in Figure 5. This procedure is based on the fact that the energies of the Gd^{3+} excited levels are much higher than the typical energy of ligand triplet states, inhibiting any ligand-to-metal energy transfer process and, therefore, the spectrum of *t*-Gd is free from LMCT bands.[87] The diffuse reflectance spectrum of *t*-Eu shows a large broad absorption band (250–550 nm) ascribed to the btfa and *t*-bpete excited states (e.g., band centered around 370–375 nm in correspondence with the observed band at 325–370 nm, band labeled as F in Figure 4) and a shoulder at 430 nm associate with the *t*-bpete ligand (curve 2 in Figure S13 in the Supporting Information), in which the $^{7}F_0 \rightarrow {}^{5}L_6$ and $^{5}D_2$ intra4f^6 transitions are superimposed. The diffuse reflectance spectrum of *t*-Gd displays only the ligands-related components (curve 5 in Figure S13 in the Supporting Information). The arithmetic difference between the two spectra (Figure S14 in the Supporting Information) reveals the presence of LMCT states peaking at 417 nm (23981 cm^{-1}) and at ~335 nm (29850 cm^{-1}) both with fwhm of ~4500 cm^{-1}. These states can be assigned to the btfa and *t*-bpete ligands, respectively, by using an approximate expression for the energy $E(\alpha)$ of a given LMCT state: $E(\alpha) \approx (-\varepsilon_\alpha) - E_A$, where ε_α is the energy of the α-orbital that approximates (Koopmans' approximation) the ionization energy of the donor (ligands) and E_A is the electron affinity of the acceptor (Eu^{3+} ion). According to the B3LYP calculations (Table S3 in the Supporting Information) the higher energy occupied orbitals (H, H − 1, and H − 2) are related to the btfa ligands, whereas the occupied orbitals associated with the *t*-bpete ligand have lower energies (H − 3 and H − 4) and contribute to the LMCT band observed at shorter wavelengths. Thus, the relative positions of the LMCT states can be assigned by the occupied orbital energies because the E_A quantity should be constant for a given compound. Importantly, the lowest lying LMCT state is very close (~1500 cm^{-1}) to that of the triplet state energy (22522.5 cm^{-1}), matching the theoretical predictions for the energy region corresponding to extremely high luminescence quenching and very low emission quantum yield,[88] in straight agreement with the observed low emission quantum yield ($\phi < 0.01$) before irradiation.

During UV irradiation, while the energy of the lowest lying LMCT deviates toward the blue that of the triplet state is red-shifted, as depicted in Figure 9. After 10 min of irradiation at 360 nm, the LMCT already peaks at 396 nm (25 253 cm^{-1}) and becomes narrow (fwhm ~3000 cm^{-1}), whereas the T_1 energy decreases to 21 635.7 cm^{-1} (462.2 nm), as shown in Figure 9 and Figures S6 and S15 in the Supporting Information. As the energy gap between the lowest lying LMCT and the T_1 state increases, the deactivation via LMCT states is reduced favoring an increase in the emission quantum yield for *t*-Eu. Notice that these two events are correlated and their kinetics are within minutes, because after 10 min the energy and fwhm values of both states remain practically constant (Figure S15 in the Supporting Information). This kinetics is consistent with the proposed trans-to-cis isomerization mechanism under hindered stereochemistry and steric restrictions. Furthermore, these observations and remarks are corroborated by the vibrational spectra (Figures S7 and S8 in the Supporting
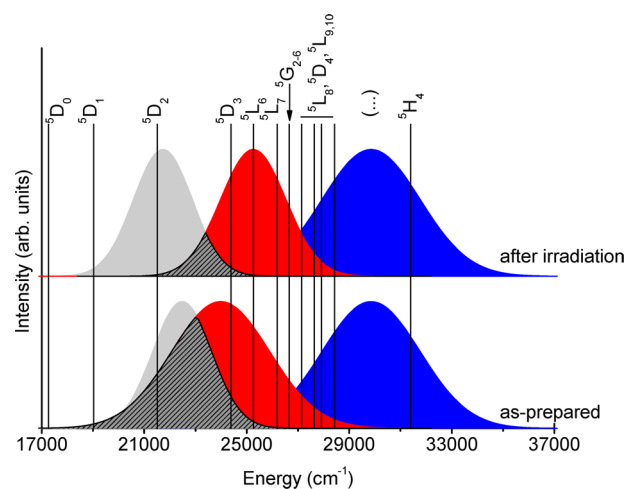
Figure 9. Scheme illustrating the overlap between the LMCT states (red and blue Gaussian bands), the triplet T_1 state (light gray Gaussian band) and selected intra-$4f^6$ levels (vertical lines) before (as-prepared) and after irradiation (at 360 nm for 10 min). The shadow area (dark gray) highlights the overlap between T_1 and the lowest energy LMCT state.

Information) and calculated electronic structures (Figure 3 and Table S3 in the Supporting Information) of the *t*-**Eu** and *c*-**Eu** monomers. Noteworthy that the energy decrease of the lowest-lying triplet upon the trans-to-cis transformation is predicted by the calculations and can be explained by the change of the nature of the LUMO, as observed in Figure 3. Whereas in *t*-**Eu** LUMO is localized at the *t*-bpete ligand, in *c*-**Eu** it has a dominant contribution from the btfa ligand. Also, the increase of the lowest-lying LMCT energy can be explained by the change of the acceptor states due to the modifications of the nature (contributions of distinct ligands) of the occupied and unoccupied orbitals, as well as the variations of the coordination polyhedron induced by trans-to-cis transformation, as observed in the calculated structures of *t*-**Eu** and *c*-**Eu**

CONCLUSIONS

Photostable under UV irradiation (>330 nm) β-diketonate-based complexes (*t*-**Eu** and *t*-**Gd**) with photoactive *t*-bpete ligand were synthesized and structural and spectroscopically characterized. Additionally, quantum chemical calculations were performed supporting the interpretation and rationalization of the experimental results. A mechanism based on a photoclick trans-to-cis-trans isomerization of both *t*- and *c*-bpete moieties was proposed to explain the unusual observed photostability of these compounds.

All experimental observations and quantum chemical calculations indicate that *t*-**Eu** and *t*-**Gd** undergo a trans-to-cis photoisomerization of the bpete ligand under UV irradiation either in solid state or in solution. This transformation is likely to be responsible for the observed photostability of these compounds, namely, the isomerization process absorbs the incident radiation and diverts it from other deleterious photochemical or photophysical process that causes the typical photobleaching process of β-diketonate chelates trivalent lanthanides. The photostability is maintained because once the *t*-bpete is transformed to *c*-bpete, this also can be isomerized back, so that the system reaches a photostationary state continuously absorbing radiation and channeling it to this transformation. For crystalline samples, this transformation is

likely to occur only near the surface because the large motion required for the trans-to-cis isomerization might be compensate by surface reconstruction.

The relevance of the double-bond in the bpete ligand on the photostability of the systems based on this ligand can be ascertain by comparing with a similar ligand, 1,2-bis(4-pyridyl)ethane (bpeta), that also bridges two lanthanide moieties in the crystal structure.[23] Indeed, both systems are similar regarding the overall dimeric structure and coordination environment of the lanthanide ions. The main distinction is the presence of a double-bond with trans stereochemistry in *t*-bpete that is absence in the bpeta ligand. However, their photostability toward UV irradiation are completely different. The complex based on bpeta presents the typical photobleaching of Ln^{3+}-based β-diketonate chelates (which is improved when incorporated into hybrid matrices[23]), whereas the protection toward degradation under UV radiation provided by the trans-cis isomerization photostationary state of the bpete ligand renders the *t*-**Eu** and *t*-**Gd** compounds photostable. For the particular case of *t*-**Eu**, this isomerization also leads a significant enhancement of the emission intensity and the quantum yield due to the confluence of the following factors: (i) an increase of the absorption cross-section; (ii) an increase of the energy gap between the lowest lying triplet state and the quenching pathway through the LMCT state; and (iii) the narrowing of the lowest-lying LMCT fwhm. Indeed, this isomerization process could be extended to other chelate ligands/complexes permitting the design of new lanthanide-based photostable systems under UV exposure for wider practical use in lighting, sensing, and displays.

ASSOCIATED CONTENT

S **Supporting Information**

Tables S1−S6 and Figures S1−S15. This material is available free of charge via the Internet at http://pubs.acs.org.

AUTHOR INFORMATION

Corresponding Author

*E-mail: lcarlos@ua.pt (L.D.C.); longo@ufpe.br (R.L.L.).

Notes

The authors declare no competing financial interest.

ACKNOWLEDGMENTS

REFERENCES

(1) Bassett, A. P.; Magennis, S. W.; Glover, P. B.; Lewis, D. J.; Spencer, N.; Parsons, S.; Williams, R. M.; de Cola, L.; Pikramenou, Z. *J. Am. Chem. Soc.* **2004**, *126*, 9413.

(2) Binnemans, K. In *Handbook on the Physics and Chemistry of Rare Earths*; Gschneidner Jr., K. A., Bünzli, J.-C. G., Pecharsky, V. K., Eds.; Elsevier: Amsterdam, 2005; Vol. 35, p 107.

(3) de Sá, G. F.; Malta, O. L.; Donegá, C. D.; Simas, A. M.; Longo, R. L.; Santa-Cruz, P. A.; da Silva, E. F. *Coord. Chem. Rev.* **2000**, *196*, 165.

(4) Lima, P. P.; Malta, O. L.; Alves, S. *Quim. Nova* **2005**, *28*, 805.

(5) Bünzli, J.-C. G. *Acc. Chem. Res.* **2005**, *39*, 53.

(6) Jiang, J.; Higashiyama, N.; Machida, K.-I.; Adachi, G.-Y. *Coord. Chem. Rev.* **1998**, *170*, 1.

(7) Renaud, F.; Piguet, C.; Bernardinelli, G.; Bünzli, J.-C. G.; Hopfgartner, G. *J. Am. Chem. Soc.* **1999**, *121*, 9326.

(8) Xu, J. D.; Corneillie, T. M.; Moore, E. G.; Law, G. L.; Butlin, N. G.; Raymond, K. N. *J. Am. Chem. Soc.* **2011**, *133*, 19900.

(9) Quang, A. Q. L.; Truong, V. G.; Jurdyc, A. M.; Jacquier, B.; Zyss, J.; Ledoux, I. *J. Appl. Phys.* **2007**, *101*, 023110.

(10) Polman, A.; van Veggel, F. C. J. M. *J. Opt. Soc. Am. B* **2004**, *21*, 871.

(11) Quirino, W.; Reyes, R.; Legnani, C.; Nobrega, P. C.; Santa-Cruz, P. A.; Cremona, M. *Synth. Met.* **2011**, *161*, 964.

(12) Charbonnière, L. J.; Hildebrandt, N.; Ziessel, R. F.; Loehmannsroeben, H. G. *J. Am. Chem. Soc.* **2006**, *128*, 12800.

(13) Graffion, J.; Cattoën, X.; Wong Chi Man, M.; Fernandes, V. R.; André, P. S.; Ferreira, R. A. S.; Carlos, L. D. *Chem. Mater.* **2011**, *23*, 4773.

(14) Norek, M.; Kampert, E.; Zeitler, U.; Peters, J. A. *J. Am. Chem. Soc.* **2008**, *130*, 5335.

(15) Brites, C. D. S.; Lima, P. P.; Silva, N. J. O.; Millán, A.; Amaral, V. S.; Palacio, F.; Carlos, L. D. *Adv. Mater.* **2010**, *22*, 4499.

(16) Moore, E. G.; Samuel, A. P.; Raymond, K. N. *Acc. Chem. Res.* **2009**, *42*, 542.

(17) Eliseeva, S. V.; Bünzli, J.-C. G. *Chem. Soc. Rev.* **2010**, *39*, 189.

(18) Armelao, L.; Quici, S.; Barigelletti, F.; Accorsi, G.; Bottaro, G.; Cavazzini, M.; Tondello, E. *Coord. Chem. Rev.* **2010**, *254*, 487.

(19) Pagnot, T.; Audebert, P.; Tribillon, G. *Chem. Phys. Lett.* **2000**, *322*, 572.

(20) Gameiro, C. G.; da Silva, E. F.; Alves, S.; de Sá, G. F.; Santa-Cruz, P. A. *J. Alloys Compd.* **2001**, *323*, 820.

(21) Nockemann, P.; Beurer, E.; Driesen, K.; Van Deun, R.; Van Hecke, K.; Van Meervelt, L.; Binnemans, K. *Chem. Commun.* **2005**, 4354.

(22) Lima, P. P.; Ferreira, R. A. S.; Freire, R. O.; Paz, F. A. A.; Fu, L. S.; Alves, S.; Carlos, L. D.; Malta, O. L. *Chem. Phys. Chem.* **2006**, *7*, 735.

(23) Lima, P. P.; Paz, F. A. A.; Ferreira, R. A. S.; de Zea Bermudez, V.; Carlos, L. D. *Chem. Mater.* **2009**, *21*, 5099.

(24) Songzhu, L.; Xiangting, D.; Jinxian, W.; Guixia, L.; Wenshen, Y.; Ruokun, J. *Spectrochim. Acta A* **2010**, *77*, 885.

(25) Kai, J. A.; Felinto, M. C. F. C.; Nunes, L. A. O.; Malta, O. L.; Brito, H. F. *J. Mater. Chem.* **2011**, *21*, 3796.

(26) Meshkova, S. B.; Topilova, Z. M.; Nazarenko, N. A.; Litvinenko, A. V.; Efryushina, N. P. *J. Anal. Chem.* **2004**, *59*, 246.

(27) Zhang, H.; Xu, Y.; Yang, W.; Li, Q. G. *Chem. Mater.* **2007**, *19*, 5875.

(28) Huang, X. G.; Wang, Q.; Yan, X. H.; Xu, J.; Liu, W. S.; Wang, Q.; Tang, Y. *J. Phys. Chem. C* **2011**, *115*, 2332.

(29) Klonkowski, A. M.; Szalkowska, I.; Lis, S.; Pietraszkiewicz, M.; Hnatejko, Z. *J. Lumin.* **2005**, *115*, 122.

(30) Souza, A. P.; Rodrigues, L. C. V.; Brito, H. F.; Alves, S.; Malta, O. L. *Inorg. Chem. Commun.* **2012**, *15*, 97.

(31) Xu, Q.; Li, L.; Liu, X.; Xu, R. *Chem. Mater.* **2002**, *14*, 549.

(32) Carlos, L. D.; Ferreira, R. A. S.; de Zea Bermudez, V.; Ribeiro, S. J. L. *Adv. Mater.* **2009**, *21*, 509.

(33) Carlos, L. D.; Donegá, C. D.; Albuquerque, R. Q.; Alves, S.; Menezes, J. F. S.; Malta, O. L. *Mol. Phys.* **2003**, *101*, 1037.

(34) Li, S.; Song, H.; Li, W.; Ren, X.; Lu, S.; Pan, G.; Fan, L.; Yu, H.; Zhang, H.; Qin, R.; Dai, Q.; Wang, T. *J. Phys. Chem. B* **2006**, *110*, 23164.

(35) Gameiro, C. G.; da Silva, E. F.; Alves, S.; de Sá, G. F.; Santa-Cruz, P. A. *Mater. Sci. Forum* **1999**, *315–317*, 249.

(36) Hasegawa, Y.; Nakagawa, T.; Kawai, T. *Coord. Chem. Rev.* **2010**, *254*, 2643.

(37) Yu, J. B.; Sun, L. N.; Peng, H. S.; Stich, M. I. J. *J. Mater. Chem.* **2010**, *20*, 6975.

(38) Yan, Q.; Wu, Y. P.; Han, K.; Luo, Y. H.; Zhang, Q. J. *Spectrochim. Acta A* **2010**, *75*, 992.

(39) Binnemans, K. *J. Mater. Chem.* **2009**, *19*, 448.

(40) Kłonkowski, A. M.; Grobelna, B.; But, S.; Lis, S. *J. Non-Cryst. Solids* **2006**, *352*, 2213.

(41) Yan, B.; Wang, Q. M. *Cryst. Growth Des.* **2008**, *8*, 1484.

(42) Fukuda, T.; Yamauchi, S.; Honda, Z.; Kamata, N.; Kijima, N. *Phys. Status Solidi, Rapid Res. Lett.* **2009**, *3*, 296.

(43) Carlos, L. D.; Ferreira, R. A. S.; de Zea Bermudez, V.; Julián-López, B.; Escribano, P. *Chem. Soc. Rev.* **2011**, *40*, 536.

(44) Xu, J.; Ma, Y. F.; Jia, L.; Huang, X. G.; Deng, Z. M.; Wang, H. P.; Liu, W. S.; Tang, Y. *Mater. Chem. Phys.* **2012**, *133*, 78.

(45) Ding, Y. X.; Wang, Y. G.; Li, H. R.; Duan, Z. Y.; Zhang, H. H.; Zheng, Y. X. *J. Mater. Chem.* **2011**, *21*, 14755.

(46) Zhao, C.; Feng, L.; Xu, B.; Ren, J.; Qu, X. *Chem.—Eur. J.* **2011**, *17*, 7007.

(47) Maggini, L.; Toma, F. M.; Feruglio, L.; Malicka, J. M.; Da Ros, T.; Armaroli, N.; Prato, M.; Bonifazi, D. *Chem.—Eur. J.* **2012**, *18*, 5889.

(48) Dugave, C.; Demange, L. *Chem. Rev.* **2003**, *103*, 2475.

(49) Levine, B. G.; Martinez, T. J. *Annu. Rev. Phys. Chem.* **2007**, *58*, 613.

(50) Yarkony, D. R. *Acc. Chem. Res.* **1998**, *31*, 511.

(51) Carey, F. A.; Sundberg, R. J. *Advanced Organic Chemistry, Part A: Structure and Mechanisms*; Springer Science: New York, 2007.

(52) Vreven, T.; Bernardi, F.; Garavelli, M.; Olivucci, M.; Robb, M. A.; Schlegel, H. B. *J. Am. Chem. Soc.* **1997**, *119*, 12687.

(53) Hunt, P. A.; Robb, M. A. *J. Am. Chem. Soc.* **2005**, *127*, 5720.

(54) Turro, N. J. *Modern Molecular Photochemistry*; University Science Books: Sausalito, CA, 1991.

(55) Kottke, T.; Stalke, D. *J. Appl. Crystallogr.* **1993**, *26*, 615.

(56) *APEX2 Data Collection Software*, version 2.1-RC13; Bruker AXS: Delft, The Netherlands, 2006.

(57) *Cryopad Remote Monitoring and Control*, version 1.451; Oxford Cryosystems: Oxford, United Kingdom, 2006.

(58) *SAINT+ Data Integration Engine*, version 7.23a; Bruker AXS: Madison, Wisconsin, USA, 1997−2005.

(59) Sheldrick, G. M. *SADABS, Bruker/Siemens Area Detector Absorption Correction Program* version 2.01; Bruker AXS: Madison, Wisconsin, USA, 1998.

(60) Sheldrick, G. M. *SHELXS-97, Program for Crystal Structure Solution*; University of Göttingen: Göttingen, The Netherlands, 1997.

(61) Sheldrick, G. M. *Acta Crystallogr. A* **2008**, *64*, 112.

(62) Sheldrick, G. M. *SHELXL-97, Program for Crystal Structure Refinement*; University of Göttingen: Göttingen, The Netherlands, 1997.

(63) Brandenburg, K. *DIAMOND*, version 3.2f; Crystal Impact GbR: Bonn, Germany, 1997−2010.

(64) Gutierrez, F.; Tedeschi, C.; Maron, L.; Daudey, J. P.; Poteau, R.; Azema, J.; Tisnes, P.; Picard, C. *Dalton Trans.* **2004**, 1334.

(65) Guillaumont, D.; Bazin, H.; Benech, J. M.; Boyer, M.; Mathis, G. *Chem. Phys. Chem.* **2007**, *8*, 480.

(66) de Silva, C. R.; Li, J.; Zheng, Z.; Corrales, L. R. *J. Phys. Chem. A* **2008**, *112*, 4527.

(67) D'Aleo, A.; Picot, A.; Beeby, A.; Gareth Williams, J. A.; Le Guennic, B.; Andraud, C.; Maury, O. *Inorg. Chem.* **2008**, *47*, 10258.

(68) Li, X. N.; Wu, Z. J.; Si, Z. J.; Liang, Z.; Liu, X. J.; Zhang, H. J. *Phys. Chem. Chem. Phys.* **2009**, *11*, 9687.

(69) Nolasco, M. M.; Vaz, P. D.; Carlos, L. D. *New J. Chem.* **2011**, *35*, 2435.

(70) Dolg, M.; Stoll, H.; Savin, A.; Preuss, H. *Theor. Chim. Acta* **1989**, *75*, 173.

(71) Stratmann, R. E.; Scuseria, G. E.; Frisch, M. J. *J. Chem. Phys.* **1998**, *109*, 8218.

(72) Tomasi, J.; Persico, M. *Chem. Rev.* **1994**, *94*, 2027.

(73) Frisch, M. J.; Trucks, G. W.; Schlegel, H. B.; Scuseria, G. E.; Robb, M. A.; Cheeseman, J. R.; Montgomery, J. A., Jr.; Vreven, T.; Kudin, K. N.; Burant, J. C.; Millam, J. M.; Iyengar, S. S.; Tomasi, J.; Barone, V.; Mennucci, B.; Cossi, M.; Scalmani, G.; Rega, N.;

597

dx.doi.org/10.1021/cm303776x | *Chem. Mater.* 2013, 25, 586−598

Petersson, G. A.; Nakatsuji, H.; Hada, M.; Ehara, M.; Toyota, K.; Fukuda, R.; Hasegawa, J.; Ishida, M.; Nakajima, T.; Honda, Y.; Kitao, O.; Nakai, H.; Klene, M.; Li, X.; Knox, J. E.; Hratchian, H. P.; Cross, J. B.; Bakken, V.; Adamo, C.; Jaramillo, J.; Gomperts, R.; Stratmann, R. E.; Yazyev, O.; Austin, A. J.; Cammi, R.; Pomelli, C.; Ochterski, J. W.; Ayala, P. Y.; Morokuma, K.; Voth, G. A.; Salvador, P.; Dannenberg, J. J.; Zakrzewski, V. G.; Dapprich, S.; Daniels, A. D.; Strain, M. C.; Farkas, O.; Malick, D. K.; Rabuck, A. D.; Raghavachari, K.; Foresman, J. B.; Ortiz, J. V.; Cui, Q.; Baboul, A. G.; Clifford, S.; Cioslowski, J.; Stefanov, B. B.; Liu, G.; Liashenko, A.; Piskorz, P.; Komaromi, I.; Martin, R. L.; Fox, D. J.; Keith, T.; Al-Laham, M. A.; Peng, C. Y.; Nanayakkara, A.; Challacombe, M.; Gill, P. M. W.; Johnson, B.; Chen, W.; Wong, M. W.; Gonzalez, C.; Pople, J. A. *Gaussian 03*; Gaussian, Inc.: Wallingford CT, 2004.

(74) Gallardo, H.; Conte, G.; Tuzimoto, P.; Bortoluzzi, A.; Peralta, R. A.; Neves, A. *Inorg. Chem. Commun.* **2008**, *11*, 1292.

(75) Zhang, Y.; Li, C.; Shi, H. H.; Du, B.; Yang, W.; Cao, Y. *New J. Chem.* **2007**, *31*, 569.

(76) Polo, A. S.; Itokazu, M. K.; Frin, K. M.; Patrocínio, A. O. T.; Murakami Iha, N. Y. *Coord. Chem. Rev.* **2006**, *250*, 1669.

(77) Patrocínio, A. O. T.; Murakami Iha, N. Y. *Inorg. Chem.* **2008**, *47*, 10851.

(78) Gutierrez, A. R.; Whitten, D. G. *J. Am. Chem. Soc.* **1974**, *96*, 7128.

(79) Busby, M.; Matousek, P.; Towrie, M.; Vlcek, A. *J. Phys. Chem. A* **2005**, *109*, 3000.

(80) Dattelbaum, D. M.; Itokazu, M. K.; Murakami Iha, N. Y.; Meyer, T. J. *J. Phys. Chem. A* **2003**, *107*, 4092.

(81) Bossert, J.; Daniel, C. *Chem.—Eur. J.* **2006**, *12*, 4835.

(82) Itokazu, M. K.; Polo, A. S.; de Faria, D. L. A.; Bignozzi, C. A.; Murakami Iha, N. Y. *Inorg. Chem. Acta* **2001**, *313*, 149.

(83) Wenger, O. S.; Henling, L. M.; Day, M. W.; Winkler, J. R.; Gray, H. B. *Inorg. Chem.* **2004**, *43*, 2043.

(84) Frin, K. M.; Itokazu, M. K.; Murakami Iha, N. Y. *Inorg. Chim. Acta* **2010**, *363*, 294.

(85) Frin, K. M.; Murakami Iha, N. Y. *Inorg. Chem. Acta* **2011**, *376*, 531.

(86) Liu, R. S. H. *Acc. Chem. Res.* **2001**, *34*, 555.

(87) Carlos, L. D.; Fernandes, J. A.; Ferreira, R. A. S.; Malta, O. L.; Gonçalves, I. S.; Ribeiro-Claro, P. *Chem. Phys. Lett.* **2005**, *413*, 22.

(88) Faustino, W. M.; Malta, O. L.; de Sá, G. F. *J. Chem. Phys.* **2005**, *122*, 054109.